

Practical, Reliable Error Bars in Quantum Tomography

Philippe Faist* and Renato Renner

Institute for Theoretical Physics, ETH Zurich, 8093 Switzerland

(Dated: July 5, 2016)

Precise characterization of quantum devices is usually achieved with quantum tomography. However, most methods which are currently widely used in experiments, such as maximum likelihood estimation, lack a well-justified error analysis. Promising recent methods based on confidence regions are difficult to apply in practice or yield error bars which are unnecessarily large. Here, we propose a practical yet robust method for obtaining error bars. We do so by introducing a novel representation of the output of the tomography procedure, the *quantum error bars*. This representation is (i) concise, being given in terms of few parameters, (ii) intuitive, providing a fair idea of the “spread” of the error, and (iii) useful, containing the necessary information for constructing confidence regions. The statements resulting from our method are formulated in terms of a figure of merit, such as the fidelity to a reference state. We present an algorithm for computing this representation and provide ready-to-use software. Our procedure is applied to actual experimental data obtained from two superconducting qubits in an entangled state, demonstrating the applicability of our method.

Introduction.—Recent experimental developments have demonstrated increasingly precise manipulation and control of quantum systems, paving the way towards the hopeful implementation of a quantum computer [1–12]. The successful outcome of an experiment is usually certified using quantum tomography. This is the task of inferring the quantum state of a device from statistics of measurements on many copies of the system [13–19]. Several methods perform this task and are widely used, such as maximum likelihood estimation [20, 21].

In the realistic regime where finite data are collected, the error bars provided by most methods which are widely applied in current experiments [19, 22–24] are typically ill justified and may lead to deceiving conclusions [25–27]. To remedy this problem, Blume-Kohout [27] and Christandl and Renner [28] resort to *confidence regions*. These are regions in state space of all density matrices in which the state lies with high probability. In contrast to Bayesian methods [25], the reliability statements do not depend on any prior distribution. However, confidence regions are *a priori* difficult to construct explicitly [29]. Furthermore, they are designed for worst-case scenarios and are often not representative of the intuitive extent of the error.

Our main result is a novel representation of the output of the tomography procedure—a summary of what the tomographic data tells us about the state of the system—which we call *quantum error bars*. This description is (i) concise, being given in terms of a few parameters only, (ii) intuitive, providing a fair idea of the “spread” of the error, and (iii) useful for precise statements, containing all necessary information for constructing confidence regions. Our method, in particular, inherits the mathematical robustness of the confidence region approach.

The quantum error bars are designed to mimic the role of classical error bars. Classically, an error bar typically represents the standard deviation of the distribution of a physical quantity caused by noise or statistical errors; this distribution is usually assumed to be Gaussian. Observe that, precisely, classical error bars (i) are a concise description of the error, (ii) provide a fair, intuitive idea of the “spread” of the quantity of interest, and (iii) allow us to calculate precise statements such as the required error interval to consider (e.g., 5 standard

deviations) for a specific requested certainty level (e.g., one in a million).

Our statements are formulated in terms of a figure of merit which can be chosen freely. Our method works best when the figure of merit is the fidelity to a pure target state, the expectation value of an observable, or the trace distance to any reference state. This encompasses most tomography settings.

The quantum error bars are constructed as follows. The input is the experimental data from a general quantum tomography experiment. Then we construct a particular distribution $\mu(f)$ of the chosen figure of merit f , which has the property of containing the necessary information to construct confidence regions at any confidence level using the method of Ref. [28]. We show that in a wide range of situations and for a class of figures of merit, the distribution $\mu(f)$ can be approximated by a simple analytical expression with three parameters. The quantum error bars are then straightforwardly deduced from these parameters.

We provide a simple numerical algorithm to obtain the quantum error bars from the measurement data. By fitting a numerical approximation to $\mu(f)$ with our approximate analytical model, we obtain the values of the parameters of the model which directly translate to the quantum error bars. The practicality of our method is demonstrated by applying it to experimental data from two superconducting qubits.

Our work complements a vast literature which has provided error analyses for experiments [30–42] as well as explicit schemes [43–52], by introducing the novel concept of quantum error bars. The complexity of such schemes have also been investigated [53, 54] and numerical techniques put forward [25, 55–57]. Furthermore, a number of contributions propose measurement schemes for fidelity estimation [58, 59], tomography of matrix product states [60], estimation of low-rank states [61, 62], and permutationally invariant tomography [63–65]. An experiment following such schemes would achieve target benchmarks more efficiently, and it could still be analyzed using our procedure, the latter being applicable to any measurements.

The rest of this Letter is structured as follows. First, we briefly explain our quantum tomography setup and the concept of confidence regions. We then derive our main technical

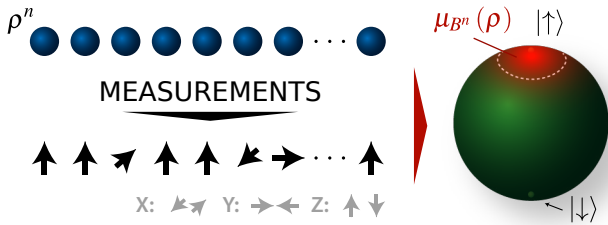


FIG. 1. Setup of quantum tomography. Measurements are taken on n copies of a quantum system. The outcomes allow us to infer what the state of the quantum system is. In this example a qubit is measured using Pauli operators. Here, the experimental data are most consistent with the state being $|\uparrow\rangle$, located at the top of the Bloch sphere (in green). However, because only finite data are collected, there is an uncertainty associated with this statement. In the method of Ref. [28], a distribution $\mu_{B^n}(\rho)$ (the red gradient) is determined from the data, from which confidence regions can be constructed (delimited by the dotted line). These are regions in state space in which the state lies with high probability.

results, namely, the definition of $\mu(f)$, its approximate theoretical model, and the algorithm to estimate $\mu(f)$ numerically. Finally, we demonstrate the applicability of our method on experimental data.

Quantum Tomography Setup.—A large number n of copies of a quantum system are measured using independent, possibly different, measurement settings (Fig. 1) [66]. We list all the of the distinct positive operator-valued measure (POVM) effects in one set $\{E_k\}$, and denote by n_k the number of times the POVM effect E_k was observed. We then construct the likelihood function, which will be needed in our analysis. It is defined as the probability with which the observed data would occur if the true state were n copies of ρ ,

$$\Lambda(\rho) = \Pr[\text{observed data} | \rho] = \prod_k (\text{tr}[E_k \rho])^{n_k}, \quad (1)$$

along with the log-likelihood,

$$\lambda(\rho) = -2 \ln \Lambda(\rho) = -2 \sum_k n_k \ln \text{tr}(E_k \rho), \quad (2)$$

with a conventional (-2) factor [27, 33].

Confidence Regions.—In the following, we briefly review the method of Ref. [28] for constructing confidence regions, on which our method is based.

Confidence regions of confidence level $1 - \varepsilon$ are defined as regions in state space which contain the true state with a probability of at least $1 - \varepsilon$. Crucially, it is the complete procedure of assigning a region to tomographic data which is certified and not the particular region itself (despite the slightly misleading terminology). More precisely, for a particular “true” state ρ_{true} , the measurement outcomes observed in the tomography procedure are only one possible outcome data set among the enormous amount of theoretically possible data sets. Now, a data analysis procedure associates with each observed data set a corresponding region in state space. This tomography procedure is said to *yield confidence regions*

of confidence level $1 - \varepsilon$ if, for any true state ρ_{true} , the tomography procedure associates with the observed data set a region which contains ρ_{true} , except for some data sets with total probability ε . In other words, the complete tomography procedure is successful except with probability ε , in which case the observed data set may cause the procedure to report a bad region. These “exceptional data sets” may be interpreted as misleading but highly unlikely situations. For example, if we flip a fair coin many times and observe the sequence of all “heads,” any reasonable inference scheme would wrongly report that the coin is highly biased. However this outcome only happens with disproportionately small probability; introducing the parameter ε above allows us to disregard such extremely unlikely cases.

The method of Ref. [28] is formulated using the *estimate density* μ_{B^n} [67], defined as

$$\mu_{B^n}(\rho) = \frac{1}{c_{B^n}} \Lambda(\rho), \quad (3)$$

where c_{B^n} is a normalizing factor such that $\int d\rho \mu_{B^n}(\rho) = 1$, and where $d\rho$ is the Hilbert-Schmidt measure normalized such that $\int d\rho = 1$ [68, 69]. The main result of Ref. [28] is a criterion for certifying a procedure for yielding confidence regions of confidence level $1 - \varepsilon$. The criterion is the following: the procedure should map to any tomographic data (essentially) a region R in state space which satisfies

$$\int_R \mu_{B^n}(\rho) d\rho = 1 - \frac{\varepsilon}{\text{poly}(n)}, \quad (4)$$

i.e., which has high weight under the distribution μ_{B^n} [70].

Confidence Regions for a Figure of Merit.—We may now use this criterion to devise an explicit procedure for constructing confidence regions, where the regions R are chosen to be defined via level sets of a figure of merit.

A figure of merit $f(\rho)$ may be any function of the quantum state. For example, $f(\rho) = F^2(\rho, |\psi_{\text{Ref}}\rangle\langle\psi_{\text{Ref}}|)$ expresses the fidelity to a reference state $|\psi_{\text{Ref}}\rangle$. The reduced distribution of the estimate density $\mu_{B^n}(\rho)$ onto the figure of merit f is given by

$$\mu(f) = \int d\rho \mu_{B^n}(\rho) \delta(f(\rho) - f), \quad (5)$$

where $\delta(\cdot)$ denotes the Dirac delta function.

Now, fix a threshold value f , and consider the region R_f in state space consisting of all states whose figure of merit is greater than or equal to f (Fig. 2). The weight of the region R_f according to the distribution $\mu_{B^n}(\rho)$ is exactly given by $\int_{f' \geq f} \mu(f') df'$. Inverting this reasoning, for any ε , we can find the maximum threshold value f required for a region R_f to encompass a particular weight $1 - \varepsilon / \text{poly}(n)$; we know that this region is essentially a confidence region by the criterion of Ref. [28]. (If the figure of merit is such that smaller values of $f(\rho)$ are desirable, such as the trace distance to a reference state, then R_f is defined with f as an upper, rather than lower, threshold value.)

We arrive at a first important observation: if we find a simple characterization of the function $\mu(f)$, then we are capable of constructing confidence regions in terms of f for any

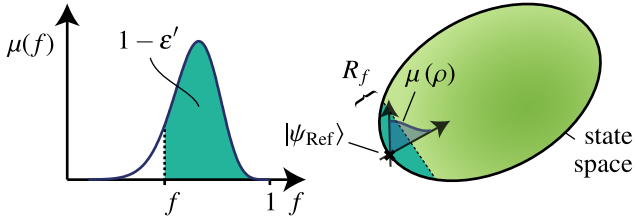


FIG. 2. Construction of confidence regions from the distribution $\mu(f)$ on the figure of merit. High weight intervals with respect to $\mu(f)$ (left plot) correspond to high weight regions in state space with respect to $\mu_{B^n}(\rho)$ (right diagram) which are (essentially) confidence regions, according to Ref. [28].

confidence level (See Appendix D for how to transpose the δ -enlargement in [28] into a shift of the threshold value f).

Determining $\mu(f)$ Numerically.—We propose a practical procedure which determines a numerical estimate of $\mu(f)$. We resort to a Monte Carlo-type scheme known as the Metropolis-Hastings algorithm [71] (cf. also Refs. [72, 73]). This algorithm is a standard, well-tested scheme widely used in computational physics—for instance, to simulate the behavior of statistical systems at finite temperature [74]—and there are standard methods for controlling the uncertainties resulting from the use of this procedure [75]. Using this algorithm, we conduct a random walk in the quantum state space and produce random samples distributed according to the distribution $\mu_{B^n}(\rho)$. By collecting the values of $f(\rho)$ at the sampled points into a histogram, we obtain an estimate for $\mu(f)$. (See Appendix A for the details of the random walk procedure).

Theoretical Model for $\mu(f)$.—It turns out that, for a selection of common figures of merit, we may understand the numerical estimate of $\mu(f)$ with a theoretical model. Suppose $f(\rho)$ is the fidelity to a pure reference state, the expectation value of an observable, or the trace distance to any reference state. Then, under some reasonable assumptions [76], we derive the following approximate theoretical model for $\mu(f)$ (see Appendix B),

$$\mu(f) \approx C (f - h)^m \cdot e^{-a_2(f-h)^2 - a_1(f-h)}, \quad (6)$$

with three fit parameters a_1 , a_2 , and m (with $m \geq 0$), and one constant normalization factor C ; h is a constant depending only on the choice of the figure of merit. Specific values of the constant h for some figures of merit are summarized in Table I.

The parameters (a_2, a_1, m) are then mapped onto new parameters which are more representative of the shape of the function. The latter is viewed as a “skewed” Gaussian (see Appendix C). The parameter f_0 determines the position of the peak, the parameter Δ is the half width of the “deskewed” Gaussian, and γ characterizes the deviation from a perfect Gaussian. The parameters (f_0, Δ, γ) are the *quantum error bars*.

Application to Experimental Data.—We have applied the

$\ln \mu(f) \approx -a_2 x^2 - a_1 x + m \ln x + c$, where:	
Figure of merit $f(\rho)$	$x =$
$F^2(\rho, \psi_{\text{Ref}}\rangle\langle\psi_{\text{Ref}}) = \langle\psi_{\text{Ref}} \rho \psi_{\text{Ref}}\rangle$	$1 - f$
$D(\rho, \rho_{\text{Ref}}) = \frac{1}{2} \ \rho - \rho_{\text{Ref}}\ _1$	f
Observable $\langle A \rangle_\rho$	$a - f$ or $f - a$

TABLE I. Theoretical fit model for some selected figures of merit. Here $|\psi_{\text{Ref}}\rangle$ denotes any pure state, and ρ_{Ref} any pure or mixed state. We use the notation $D(\rho, \sigma)$ for the trace distance and $\langle A \rangle_\rho = \text{tr}(A\rho)$ for the expectation value of an observable A . The value a is an extremal value of $\langle A \rangle_\rho$ for valid density matrices ρ close to the region of interest, and x should be chosen as $x = a - f$ (resp. $x = f - a$) if a is a maximal value (resp. minimal value). If the extremum point of A is far from the region of interest, the logarithm term in the model can be dropped, as the exponential will dominate the volume term, and a can be absorbed into the other factors.

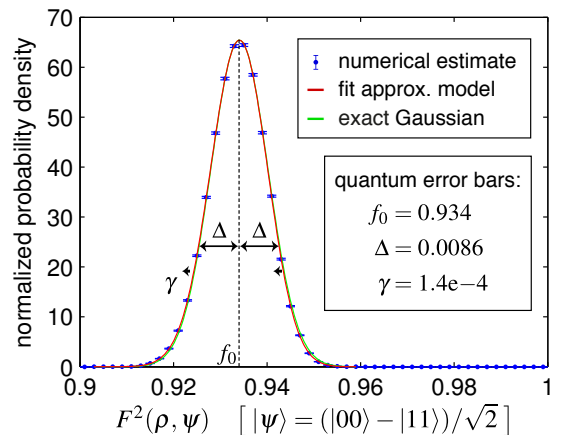


FIG. 3. Analysis of measurement data from two superconducting qubits prepared in a Bell state. We determined effective measurement operators which model the noise in the measurement process. The histogram of the fidelity to the target state $|\psi\rangle$ (the blue data points), produced using our procedure, fits well to our theoretical model in Table I. The quantum error bars are a concise, intuitive, and precise characterization of the fit model, which is interpreted as a skewed Gaussian function. The parameter f_0 is the peak maximum, Δ is the half width of the original Gaussian, and γ characterizes the skewing in terms of the displacement of the sides of the peak from the exact Gaussian at the relative height $1/e$. This example involving experimental data demonstrates a good level of practical applicability of our method.

algorithm to experimental data from two superconducting qubits prepared in a Bell state according to the setup described in Refs. [10, 77]. The data were kindly provided by the authors of Ref. [10]. The two qubits were measured using slightly noisy individual Pauli operators, with a total of $n = 55677$ measurements. The numerical estimation of $\mu(f)$ corresponding to the fidelity to the target Bell state is depicted in Fig. 3. (See Appendix F for details of the analysis of the experiment, including the modeling of the measurements [78] into effective POVM operators.)

Quantum Error Bars.—The quantum error bars (f_0, Δ, γ)

displayed in Fig. 3 are a concise and useful description of the error analysis, from which reliable operational statements can be made. Indeed, they provide the necessary information for constructing confidence regions for any given confidence level.

Also, as seen in Fig. 3, our error bars have the intuitive interpretation as representing the “spread” of the figure of merit according to $\mu(f)$. As such, the error bars are much smaller than the size of a confidence region for a small epsilon in a worst-case scenario, and they are in fact of comparable size to those obtained by bootstrapping [22, 24, 27, 41, 79] (see Appendix G).

Discussion.—Our work bridges the apparent gap between carrying out a mathematically rigorous, well-justified error analysis and using an *ad hoc* procedure yielding smaller error bars. The quantum error bars provide a convenient and precise representation of the information provided by the tomography procedure.

While the fit model for $\mu(f)$ is subject to some assumptions and approximations, it applies well to many examples studied by the authors in developing this work—for $n \sim 100$ total measurements already—and has been tested with up to five qubits. Note that the numerical procedure is not subject to these assumptions, and a deviation from the fit model could easily be noticed in some extreme examples considered (for example, with goodness-of-fit measures). A further detailed discussion on the reliability of our method is presented in Appendix H.

It is relatively straightforward to apply our method to experimental setups consisting of a few qubits. Our procedure is restricted neither to particular measurement settings nor to specific quantum states, and it applies, for example, to adaptive tomography. In general, noise in the measurement procedure has to be modeled into effective POVM effects analogously to our approach for the two superconducting qubits. (In contrast, other approaches do not require this [80–82].) We have developed a software which implements our procedure [83] that is expected to be directly applicable to most experimental settings.

For worst-case scenarios such as quantum cryptography [84], it is still desirable to improve the methods for explicitly constructing confidence regions. We do anticipate that the bounds used in Ref. [28] may be tightened to yield smaller confidence regions for the same confidence level. If the construction is not altered, the procedure presented here would not require any change, as the same histograms may still serve for constructing confidence regions using the tightened proof.

We also insist that our results do not rely on any particular interpretation of “probability,” such as a Bayesian or a frequentist one. This is because we consider experiments which can, *in principle*, be repeated arbitrarily many times, which is a regime where these interpretations are equivalent [28]. Nonetheless, the Bayesian viewpoint is convenient, as the distribution $\mu(f)$ happens to coincide with the Bayesian posterior corresponding to an agent starting the tomography procedure with a Hilbert-Schmidt uniform prior.

Furthermore, even though our results are formulated in the context of quantum state tomography, the same procedure

may be applied to quantum process tomography [85, 86]. Indeed, the Choi-Jamiołkowski isomorphism implies that determining a quantum process is mathematically the same as determining a bipartite quantum state.

Acknowledgments.—We thank Robin Blume-Kohout, Matthias Christandl, Steve Flammia, Aleksejs Fomins, Olivier Landon-Cardinal, Romain Müller, Denis Rosset, Cyril Stark, Lars Steffen, and Takanori Sugiyama for fruitful discussions. We acknowledge support from the European Research Council (ERC) via Grant No. 258932, from the Swiss National Science Foundation through the National Centre of Competence in Research “Quantum Science and Technology” (QSIT), and by the European Commission via the project “RAQUEL.”

SUPPLEMENTAL MATERIAL

In this appendix, we provide a detailed description of how our method is implemented, how it is applied to practical examples, as well as additional discussions referred to from the main text. An overview of our method is given in Fig. 4.

Our software, along with instructions for download and use, may be downloaded at the location: <https://tomographer.github.io/tomographer>.

Appendix A: Procedure for determining $\mu(f)$ using a Metropolis-Hastings random walk

The figure of merit is given as a function $f(\rho)$ of the quantum state. For example, the squared fidelity to a reference state ρ_{Ref} is represented as $f(\rho) = F^2(\rho, \rho_{\text{Ref}})$.

Recall that the relevant object in the method of Christandl and Renner is the *estimate density* $\mu_{B^n}(\rho)$, given by Eq. (3) of the main text.

Given the figure of merit $f(\rho)$ of interest, the reduced distribution on this of merit of $\mu_{B^n}(\rho)$ is

$$\mu(f) = \int d\rho \mu_{B^n}(\rho) \delta[f(\rho) - f], \quad (\text{A1})$$

where the Dirac delta ensures the integration is performed over the shell of states in state space which have the given figure of merit f . The quantity $\mu(f)$ corresponds to the total weight given by $\mu_{B^n}(\rho)$ to all states with a given fixed figure of merit f .

In the following, we develop a method to compute $\mu(f)$ numerically. We resort to a Monte Carlo-type scheme known as the Metropolis-Hastings algorithm [71] (cf. also Refs. [72, 73]). This scheme is widely used in computational physics, for instance to simulate the behavior of statistical systems at finite temperature [74]. This algorithm conducts a random walk which produces random samples distributed according to a given distribution $P(x)$. The parameters of the algorithm are a starting point x_0 as well as a “jump distribution” $Q(x'|x)$. The jump distribution is assumed to be symmetric ($Q(x'|x) = Q(x|x')$), and is used to update the current step in the random walk. (For example, $Q(x'|x)$ is often chosen as a Gaussian in some relevant coordinates centered at x). The i -th step of the random walk goes as follows:

1. Choose a new candidate point x' according to $Q(x'|x_i)$;
2. Calculate $a = P(x')/P(x_i)$. If $a > 1$, then set $x_{i+1} := x'$ unconditionally; if $a < 1$, then decide randomly to set $x_{i+1} := x'$ with probability a , or else to set $x_{i+1} := x_i$.

The sequence of points $\{x_i\}$, albeit correlated, are then asymptotically distributed according to the distribution $P(x)$.

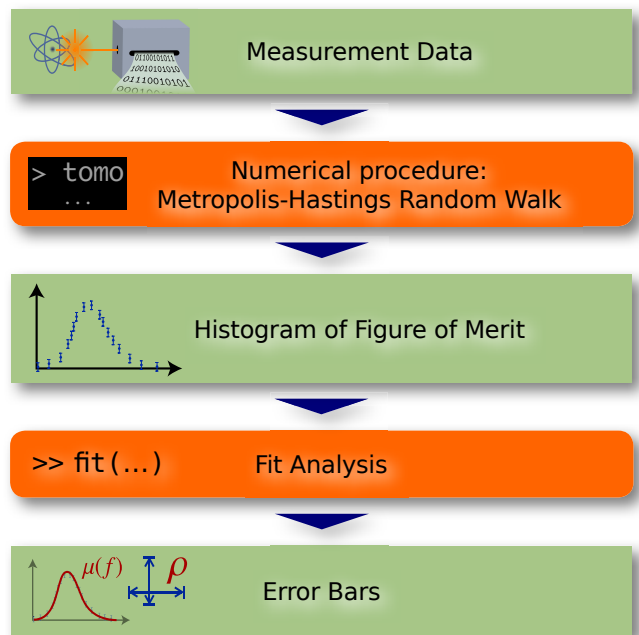


FIG. 4. Overview of our quantum tomography analysis and how to apply our method. The measurement data are the input to our procedure. Our numerical method, which is based on a Metropolis-Hastings random walk in state space, outputs a histogram of a chosen figure of merit. We provide software accomplishing this [83]. This histogram is a numerical approximation to the distribution $\mu(f)$ of the figure of merit. In a second step, this numerical estimate is fitted by a theoretical model. The fit can be done, for instance, using MATLAB. This yields a full description of the relevant distribution which allows to construct in principle confidence regions for any confidence level. This description is given in terms of three parameters, which are then effectively the “error bars.”

In order to calculate the quantity $\mu(f)$, we draw a large number of random samples in the quantum state space according to the distribution $\mu_{B^n}(\rho)$, i.e. with $\mu_{B^n}(\rho)$ playing the role of $P(x)$. The histogram of values $f(\rho)$ evaluated at those samples then provide a numerical estimate of $\mu(f)$. Crucially, it is not necessary to calculate the normalization constant c_{B^n} in the definition of μ_{B^n} (Eq. (3) of the main text) because in the Metropolis-Hastings algorithm we only have to evaluate ratios of probabilities.

For our random walk, we represent a quantum state ρ of dimension d by a square complex matrix T with $\text{tr}TT^\dagger = 1$, such that $\rho = TT^\dagger$. To any such T corresponds a valid density matrix ρ , and to any density matrix ρ corresponds at least one such T (e.g. $T = \rho^{1/2}$). Additionally, the constraint $\text{tr}TT^\dagger = 1$ corresponds to requiring that the components of T , real and imaginary parts taken separately into a real vector \vec{y} , lie on the surface of the unit $(2d^2 - 1)$ -hypersphere. Random density matrices may be sampled from the Hilbert-Schmidt measure by choosing such random points on this hypersphere [68]. In fact, the matrix entries T_{ij} of T are simply the components of a vector $|\psi\rangle$ of dimension d^2 which purifies ρ . Indeed, if we trace out the second system from $|\psi\rangle = \sum_{ij} T_{ij} |i\rangle_A \otimes$

$|j\rangle_B$, we obtain $\text{tr}_B|\psi\rangle\langle\psi| = \sum_{ij'} T_{ij'} T_{ij'}^* |i\rangle\langle i'| = TT^\dagger = \rho$. We hence choose to perform a Metropolis-Hastings random walk on the $(2d^2 - 1)$ -hypersphere corresponding to the possible T matrices. The jump candidate is calculated from a point \bar{y}_i by choosing a vector $\bar{\omega}$ of $2d^2$ normally distributed values and setting $\bar{y}' = (\bar{y}_i + \eta_{\text{step}}\bar{\omega}) / \|\bar{y}_i + \eta_{\text{step}}\bar{\omega}\|$, where η_{step} is a chosen step size. The jump distribution obtained in this way is symmetric.

We follow the the prescriptions given in Ref. [75] for the correct usage and appropriate error analysis of the Metropolis-Hastings algorithm. First, since the random starting point is likely to be a point which has very little weight under $P(x)$, the random walk needs to equilibrate, or thermalize, until it reaches points which have a non-negligible values of $P(x)$. This first set of points traversed until the walk has thermalized should be discarded. Also, because consecutively collected samples may be very correlated, it is useful to keep only one sample in a certain number N_{sweep} (the ‘‘sweep size’’), while throwing away each time the $N_{\text{sweep}} - 1$ points between two recorded samples. In our examples, the sweep size N_{sweep} is chosen of the order of $1/\eta_{\text{step}}$; this gives at least the chance to the random walk to traverse all of state space between two recorded samples. Errors on the final numerical histogram points may be estimated either by calculating the standard deviation of independent runs of the simulation, or by a binning analysis which takes into account the correlation of the samples during a single run. We refer to Ref. [75] for a detailed discussion of these techniques.

In our case, for each histogram bin, we associate to each recorded sample the value 1 if the point is in the bin, or 0 otherwise. The final numerical estimate of $\mu(f)$ is produced by averaging the time series for each bin, which corresponds up to a constant to generating a histogram of counts. These time series are suitable for use in a binning analysis to obtain error bars on the numerical estimate of $\mu(f)$.

Appendix B: The fit model for $\mu(f)$

We now derive an approximate theoretical model to fit our numerical histogram. This is useful in order to provide a succinct description of the result in terms of only a few parameters. It also serves as a consistency check allowing us to assert that our results are well understood from a theoretical point of view.

In general, the function $\mu(f)$ can be very complicated, so an exact analytical description is unlikely. Rather, our goal is to find a decent approximation of this function in a region close to where μ_{B^n} has high weight.

In fact, the bell shape of the curves in Fig. 3 of the main text is typical when the figure of merit is taken to be the fidelity to a pure target state, the expectation value of an observable or the trace distance to any reference state. Intuitively, this shape is the result of the concurrence of two effects: a volume factor reflecting the increasing surface of a shell of fixed figure of merit as we get far from the reference point, and the approximately exponential decrease of the likelihood function itself. For example, in the case of the trace distance to the maximum

likelihood estimate, there are many more states with high distance to $\hat{\rho}_{\text{MLE}}$ than there are very close—this is the increasing volume factor. The following derivation makes this argument more precise.

Let’s now derive the fit model. We parameterize ρ with a generalized Bloch vector [87, 88]. Take an orthonormal basis $\{A_j\}$ of the Lie algebra $su(d)$, with $j = 1, \dots, M$ and $M = d^2 - 1$. The A_j are hermitian, traceless and obey $\text{tr}A_j A_{j'} = \delta_{jj'}$ (an example are the normalized generalized Gell-Mann matrices [87, 88], or, for k qubits, the normalized tensor product of Pauli operators). We may now write a general state ρ as $\rho(a_j) = (1/d)\mathbb{1} + \sum_j a_j A_j$ with real coefficients a_j obeying some nontrivial constraints such that $\rho \geq 0$. The Hilbert-Schmidt distance is given by the Euclidean distance of the generalized Bloch vectors, $\text{tr}[(\rho(a_j) - \rho(b_j))^2] = \sum_j (a_j - b_j)^2$. Now because the Hilbert-Schmidt measure $d\rho$ is induced by the Hilbert-Schmidt metric [68, 69], we may write (A1) as

$$\mu(f) = \frac{1}{c'} \int d^M a_j e^{-\frac{1}{2}\lambda(a_j)} \delta[f(a_j) - f], \quad (\text{B1})$$

with a new constant c' and $\lambda(\rho) = -2\ln\Lambda(\rho)$, and where implicitly the arguments to $\lambda(\cdot)$ and $f(\cdot)$ are to be transformed into ρ appropriately.

The conditions that the a_j have to satisfy in order to represent a positive semidefinite matrix are complicated [87, 89, 90]. However, it turns out that we don’t need to know the exact form of these constraints. Rather, we assume that:

- (i) f has an extremal value close to the region of interest (*viz.*, near ρ_{MLE});
- (ii) the surface of a shell of states of a given figure of merit f tends to zero as f tends to this extremal value.

These assumptions are rather natural and are indeed automatically satisfied if $f(\rho)$ is one of the cases considered in the main text (the squared fidelity to a pure reference state, the trace distance to a reference state ρ_{Ref} , or the expectation value of an observable). In the case of a distance measure, such as the trace distance, the extremum is usually zero at the reference state itself, and the surface of the shell of states with very small distance to ρ_{Ref} clearly shrinks to zero. In the case of the expectation value of an observable, the extremum is attained at the border of state space. Because the border of state space has no flat facets, the surface of a shell of given expectation value (a hyperplane intersected with state space) also shrinks to zero as we approach the border. Furthermore recall that the squared fidelity to a pure reference state $|\psi_{\text{Ref}}\rangle$ can be written as the expectation value of the observable $|\psi_{\text{Ref}}\rangle\langle\psi_{\text{Ref}}|$.

Denote by ρ_{Ref} a relevant reference point where the figure of merit is extremal, and let a_j^{Ref} such that $\rho_{\text{Ref}} = (1/d)\mathbb{1} + \sum_j a_j^{\text{Ref}} A_j$. (We recycle the notation ρ_{Ref} since whenever the figure of merit is a distance measure to a reference state, the same reference state is to be used here.) We go to hyperspherical coordinates (r, Ω) centered at the reference point a_j^{Ref} , with $d^M a_j = dr d\Omega r^{M-1}$, and introduce the change of vari-

ables $r \rightarrow r' = f(r, \Omega)$:

$$\begin{aligned} \mu(f) &= \frac{1}{c'} \int dr d\Omega r^{M-1} e^{-\frac{1}{2}\lambda(r, \Omega)} \delta[f(r, \Omega) - f] \\ &= \frac{1}{c'} \int dr' d\Omega \left[r^{M-1} \left| \frac{\partial f}{\partial r} \right|^{-1} \right] e^{-\frac{1}{2}\lambda(r', \Omega)} \delta[r' - f] \\ &= \frac{1}{c'} \int d\Omega \left[r^{M-1} \left| \frac{\partial f}{\partial r} \right|^{-1} \right] e^{-\frac{1}{2}\lambda(f, \Omega)}, \end{aligned} \quad (\text{B2})$$

where in the last two integrals the terms in square brackets are to be evaluated at the points r which satisfy $r' = f(r, \Omega)$ and $f = f(r, \Omega)$, respectively. Note that the figure of merit $f(r, \Omega)$ must be invertible for fixed Ω and for $r \geq 0$; this is usually the case with our choice of a_j^{Ref} above. Note also that Expression (B2) is in fact still exact, albeit very difficult to calculate explicitly. To proceed further, we will use Laplace's approximation, and assume that the main contribution to the integral is a region close to a single point Ω_0 on the shell of fixed figure of merit f where the integrand is maximal. Then, we have

$$(\text{B2}) \approx \frac{1}{c'} \left[r^{M-1} \left| \frac{\partial f}{\partial r} \right|^{-1} \right]_{\Omega_0} w[f, \Omega_0] e^{-\frac{1}{2}\lambda(f, \Omega_0)}, \quad (\text{B3})$$

where $w[f, \Omega_0]$ is a "width factor," which accounts for the total weight of the peak in Laplace's approximation, including a possible truncation of the peak caused by the border of state space. Note that the condition (ii) above for the figure of merit ensures that $w[f, \Omega_0]$ doesn't explode when f approaches the extremum of $f(\rho)$.

At this point, we need to make further assumptions about the behavior in f of the individual terms in (B3). First, we consider the regime in which the likelihood is close to Gaussian in the Hilbert-Schmidt coordinates,

$$\lambda(\vec{a}) \approx \lambda_0 + \vec{\lambda}_A \cdot (\vec{a} - \vec{a}^{\text{Ref}}) + (\vec{a} - \vec{a}^{\text{Ref}})^T \lambda_B (\vec{a} - \vec{a}^{\text{Ref}}), \quad (\text{B4})$$

(we shift \vec{a} by \vec{a}^{Ref} without loss of generality and for later practical reasons; also λ_B is a symmetric matrix). This is generically the case for most practical scenarios where a reasonable amount of measurements were taken.

Second, we need to assume something about the figure of merit $f(r, \Omega)$: we'll suppose that

$$f(r, \Omega) = r g(\Omega) + h, \quad (\text{B5})$$

where h is some known constant, and $g(\Omega)$ some function. The figures of merit considered in the main text automatically satisfy this assumption. First, if the figure of merit is any distance measure to ρ_{Ref} which is given by a norm, such as the trace distance, then $f(r, \Omega) = \|\rho(r, \Omega) - \rho_{\text{Ref}}\| = \|\sum_j (a_j(r, \Omega) - a_j^{\text{Ref}}) A_j\| = r \|\sum_j \Omega_j A_j\|$, recalling that our hyperspherical coordinates are defined by $\vec{a}(r, \Omega) = \vec{a}^{\text{Ref}} + r \vec{\Omega}$ with $\vec{\Omega}$ the unit vector in the direction Ω . Also, $f(\rho)$ obeys property (B5) if it is the expectation value of an observable, $f(\rho) = \text{tr}(\rho W)$: with $\vec{a} = r \vec{\Omega} + \vec{a}^{\text{Ref}}$ we can write $f(\rho) = \text{tr}([\mathbb{1}/d + \sum_j a_j A_j] W) = r \vec{\Omega} \cdot \vec{w} + (\vec{a}^{\text{Ref}} \cdot \vec{w} + \text{tr} W/d)$, where \vec{w} is the vector with components $w_j = \text{tr}(A_j W)$. Recall in this case that \vec{a}^{Ref} is on the border of state space. Furthermore, recall that the squared fidelity to a pure reference state can be written as the expectation value of an observable, $F^2(\rho, |\psi_{\text{Ref}}\rangle\langle\psi_{\text{Ref}}|) = \text{tr}(\rho |\psi_{\text{Ref}}\rangle\langle\psi_{\text{Ref}}|)$. However, if the figure of merit is the fidelity or purified distance to a mixed reference state, it does not satisfy in general the Ansatz (B5).

Armed with both assumptions (B4) and (B5), we see that $\partial f / \partial r = g(\Omega)$ as well as $r = (f - h) / g(\Omega)$, and we obtain

$$\begin{aligned} \mu(f) &\approx \frac{1}{c''} \left[\frac{(f-h)^{M-1}}{g^M(\Omega_0)} \right] \cdot w[f, \Omega_0] \\ &\quad \cdot e^{-\frac{1}{2}[\lambda_0 + r \vec{\lambda}_A \cdot \vec{\Omega}_0 + r^2 \vec{\Omega}_0^T \lambda_B \vec{\Omega}_0]}, \end{aligned} \quad (\text{B6})$$

where $c'' = c' \cdot \text{sign}(g(\Omega_0))$. The term in the exponential in (B6), being quadratic in r , is then also quadratic in $f - h$. At this point, we further assume that Ω_0 (where $\lambda(f, \Omega_0)$ is minimal at fixed f) is approximately constant in f , and that the term $w[f, \Omega_0]$ is either approximately constant or, being a volume factor, varies as a power of r , and thus of $f - h$. We finally obtain our fit model,

$$\mu(f) \approx C (f-h)^m \cdot e^{-a_2(f-h)^2 - a_1(f-h)}, \quad (\text{B7})$$

with 3 fit parameters a_1, a_2, m and one constant normalization factor C . The value m includes the $(M-1)$ power plus any contribution from the weight factor $w[f, \Omega]$. The expression for the logarithm of $\mu(f)$ is numerically more suitable for fitting. We thus obtain our fit model for $\ln \mu(f)$,

$$\ln \mu(f) \approx \begin{cases} -a_2(f-h)^2 - a_1(f-h) + m \ln(f-h) + c, & \text{or} \\ -a_2(h-f)^2 - a_1(h-f) + m \ln(h-f) + c, \end{cases} \quad (\text{B8a})$$

depending on whether $f \geq h$ for all valid f or $f \leq h$ for all

valid f . Indeed, either of these two conditions hold as we have

chosen the center a_j^{Ref} of our hyperspherical coordinates as an extremal point of $f(\rho)$. Table I of the main text summarizes the appropriate fit model for a selection of figure of merits.

It is further worth mentioning that for larger f , the exponential will dominate all the other terms; for example, in this regime, the details of the function $w(f, \Omega)$ is not relevant for most figures of merit.

There are certain situations in which our approximate fit model fails to accurately describe the behavior of $\mu(f)$. If too few measurements are taken, the likelihood function is not approximately Gaussian as we have assumed (however this is usually the case already for, e.g., $n \sim 100$ total measurements). Our derivation also no longer applies if Ω_0 happens to not be constant with f , or if a different figure of merit is considered such as the fidelity to a mixed reference state. Furthermore, in some cases the boundary of state space might interfere with our approximation (it might for example constrain Ω_0 causing it to vary with f), or the Laplace method might not be a good approximation if $\lambda(f, \Omega)$ has e.g. several minima for fixed f . However in examples we have studied these cases always caused our model to fit poorly to the numerical estimate in the region of the peak; we consider it very unlikely that the fit model fits the peak well but fails to describe the tail accurately. See also Appendix H for a more general discussion of the reliability of our method.

Appendix C: The quantum error bars

Now we proceed to transform the parameters (a_2, a_1, m) into more meaningful quantities, corresponding to distinctive features of the corresponding function. Consider the function

$$y(x) = -a_2 x^2 - a_1 x + m \ln(x) + c, \quad (\text{C1})$$

which for $x > 0$ exhibits a characteristic skewed bell curve as depicted in Fig. 3 of the main text. The function $y(x)$ is exactly the model for $\ln \mu(f)$, with $x = s(f - h)$ for a constant h and for a sign $s = \pm 1$ depending on the figure of merit, as given by (B8). The function (C1) can be seen as a skewed version of a parabola with summit at $(x_0, y(x_0))$ (see Figure 5a). The de-skewing operation applied to $y(x)$ consists in finding the parabola $y_{\text{deskewed}}(x) = -a(x - x_0)^2 + y_0$ with the same the peak position and curvature as $y(x)$. In other words, we find a parabola $y_{\text{deskewed}}(x)$ such that the functions $y(x)$ and $y_{\text{deskewed}}(x)$ must match at $x = x_0$ to second order. The maximum of $y(x)$ is at the point x_0 satisfying $0 = (dy/dx)|_{x_0}$, that is, $0 = -2a_2 x_0 - a_1 + m/x_0$. Solving for x_0 while ensuring that $x_0 > 0$ yields

$$x_0 = \frac{1}{4a_2} \left(-a_1 + \sqrt{a_1^2 + 8a_2 m} \right). \quad (\text{C2})$$

The condition $(d^2 y/dx^2)|_{x_0} = (d^2 y_{\text{deskewed}}/dx^2)|_{x_0}$ yields $a = a_2 + m/(2x_0^2)$. In terms of (a, x_0, y_0) , the original parameters

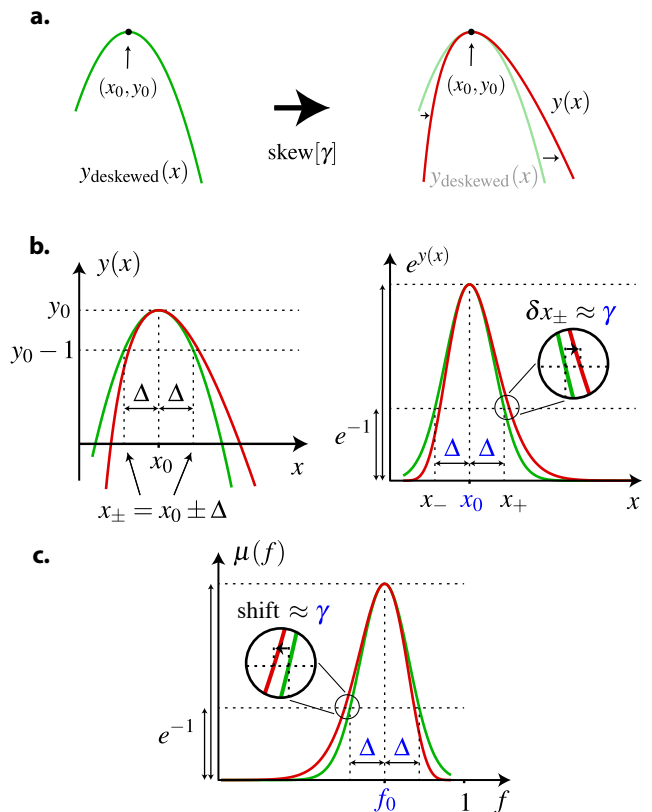


FIG. 5. Model function for $\mu(f)$ as skewed Gaussian. **a.** The function $y(x) = -a_2 x^2 - a_1 x + m \ln x + c$ (used to model $\ln \mu(f)$) can be seen as a skewed parabola, with a “skewing operation” parametrized by γ . The green curve $y_{\text{deskewed}}(x)$ is an actual parabola. **b.** The model function $y(x)$ is fully characterized by the location of the peak x_0 , the half width Δ of the “de-skewed” parabola at relative height $1/e$, and a parameter γ characterizing the shift of the sides of the peak at relative height $1/e$. **c.** The variable f relates to x via a simple shift and possible reflection, given by $x = s(f - h)$ for a constant h and $s = \pm 1$ depending on the figure of merit (see Table I of the main text). Hence, with $f_0 = s x_0 + h$, the curve $\mu(f)$ is fully characterized by the parameters (f_0, Δ, γ) , which we call the *quantum error bars*.

(a_2, a_1, c) read

$$a_2 = a - \frac{m}{2x_0^2}; \quad (\text{C3a})$$

$$a_1 = \frac{2m}{x_0} - 2a x_0; \quad (\text{C3b})$$

$$c = y_0 + a_2 x_0^2 + a_1 x_0 - m \ln x_0. \quad (\text{C3c})$$

We can already define Δ , which is the first of our quantum error bars. It is defined as

$$\Delta = \frac{1}{\sqrt{a}} = \left(a_2 + \frac{m}{2x_0^2} \right)^{-1/2}. \quad (\text{C4})$$

The parameter Δ is the half width of the Gaussian function $e^{y_{\text{deskewed}}(x)}$ at relative height $1/e$ (Figure 5b): Indeed, the standard deviation of a Gaussian is precisely the half width of the Gaussian peak at relative height $1/e$ with respect to the Gaussian peak maximum. In our case, Δ is interpreted as the half

width of the Gaussian, before the skewing operation is applied.

It remains to understand the effect of the m parameter in terms of skewing. Consider the intercepts of $y_{\text{deskewed}}(x)$ with the line $y = y_0 - \xi$, which are at $x_{\pm} = x_0 \pm \xi^{1/2}\Delta$. (These points correspond to the cross-section of the peak of $e^{y_{\text{deskewed}}(x)}$ at a relative height $e^{-\xi}$.) If we view the function $y(x)$ as the result of skewing $y_{\text{deskewed}}(x)$ via the transformation above parametrized by m , then the intercepts with the line $y = y_0 - \xi$ are shifted by some δx_{\pm} which vary as a function of m . Let us determine δx_{\pm} to first order in m . For infinitesimal m , the equation $y(x_{\pm}) = y_0 - \xi$ defining x_{\pm} varies correspondingly as $y(x_{\pm} + \delta x_{\pm}) + \delta y(x_{\pm} + \delta x_{\pm}) = y_0 - \xi$. Keeping only

the terms of first order in m we obtain

$$\left. \frac{dy}{dx} \right|_{x_{\pm}} \delta x_{\pm} + \delta y(x_{\pm}) = 0. \quad (\text{C5})$$

Noting that we only need $(dy/dx)|_{x_{\pm}}$ to zeroth order in m , we have

$$\begin{aligned} \left. \frac{dy}{dx} \right|_{x_{\pm}, m=0} &= -2a_2 x_{\pm} - a_1 = -2a x_{\pm} + 2a x_0 \\ &= \mp 2a \xi^{1/2} \Delta. \end{aligned} \quad (\text{C6})$$

Also, with $\delta a_2 = -m/(2x_0^2)$, $\delta a_1 = 2m/x_0$ and $\delta c = (\delta a_2)x_0^2 + \delta a_1 - m \ln x_0$, we have

$$\begin{aligned} \delta y(x_{\pm}) &= -(\delta a_2)x_{\pm}^2 - (\delta a_1)x_{\pm} + m \ln(x_{\pm}) + \delta c \\ &= (\delta a_2)(x_0^2 - x_{\pm}^2) + (\delta a_1)(x_0 - x_{\pm}) + m \ln \frac{x_{\pm}}{x_0} \\ &= -\frac{m}{2x_0^2} \cdot (\mp 2x_0 \xi^{1/2} \Delta - (\xi^{1/2} \Delta)^2) \mp \frac{2m}{x_0} \cdot (\xi^{1/2} \Delta) + m \ln \left(1 + \frac{\xi^{1/2} \Delta}{x_0} \right) \\ &= \mp m \frac{\xi^{1/2} \Delta}{x_0} + \frac{m(\xi^{1/2} \Delta)^2}{2x_0^2} + m \ln \left(1 \pm \frac{\xi^{1/2} \Delta}{x_0} \right). \end{aligned} \quad (\text{C7})$$

Developing the logarithm as a Taylor series in Δ , the first two orders cancel and we have

$$(\text{C7}) \approx \frac{\pm m (\xi^{1/2} \Delta)^3}{3x_0^3} - \frac{m (\xi^{1/2} \Delta)^4}{4x_0^4} + \dots + \frac{(-1)(\mp 1)^k \xi^{k/2} \Delta^k}{k \cdot x_0^k} + \dots \quad (\text{C8})$$

Then we obtain from (C5), also recalling that $a = \Delta^{-2}$,

$$\begin{aligned} \delta x_{\pm} &= -\left(\left. \frac{dy}{dx} \right|_{x_{\pm}} \right)^{-1} \cdot \delta y|_{x_{\pm}} \\ &= -(\mp 2 \xi^{1/2} \Delta^{-1})^{-1} \left(\frac{\pm m (\xi^{1/2} \Delta)^3}{3x_0^3} + \dots + \frac{(-1)(\mp 1)^k \xi^{k/2} \Delta^k}{k \cdot x_0^k} + \dots \right) \\ &= \frac{m \xi \Delta^4}{6x_0^3} \mp \frac{m \xi^{3/2} \Delta^5}{8x_0^4} + \dots + \frac{(\mp 1)^{k+1} \xi^{(k-1)/2} \Delta^{k+1}}{2k \cdot x_0^k} + \dots \end{aligned} \quad (\text{C9})$$

We now introduce the *skewing factor* γ as

$$\gamma = \frac{m \Delta^4}{6x_0^3}, \quad (\text{C10})$$

such that to lowest order in Δ , the shift of the ‘‘sides of the peak’’ given by x_{\pm} for a relative height $e^{-\xi}$ is directly proportional to γ (see also Figure 5b):

$$\delta x_{\pm} \approx \xi \gamma. \quad (\text{C11})$$

More precisely, the shift for infinitesimal m is given by

$$\delta x_{\pm} = \gamma \cdot \left(\xi \mp \frac{3 \xi^{3/2} \Delta}{4x_0} + \dots + \frac{(\mp 1)^{k'} \cdot 3 \cdot \xi^{(k'/2)+1} \Delta^{k'}}{(k'+3) \cdot x_0^{k'}} + \dots \right). \quad (\text{C12})$$

We may straightforwardly define $f_0 = s x_0 + h$ as the position of the peak in terms of the figure of merit f , by invoking the relation $x = s(f - h)$ which we used to write (C1). Finally, we obtain a set of parameters (f_0, Δ, γ) , along with a normalization constant y_0 , which now all have a direct interpretation in terms of features of the modeled distribution (Figure 5c).

In summary, they are given in terms of the fitted parameters (a_2, a_1, m) as:

$$f_0 = h + \frac{s}{4a_2} \left(-a_1 + \sqrt{a_1^2 + 8a_2 m} \right); \quad (\text{C13a})$$

$$\Delta = \left(a_2 + \frac{m}{2x_0^2} \right)^{-1/2}; \quad (\text{C13b})$$

$$\gamma = m \cdot \frac{\Delta^4}{6x_0^3}, \quad (\text{C13c})$$

recalling that $s = \pm 1$ and h in the relation $x = s(f - h)$ are fixed by the choice of figure of merit, as given in Table I of the main text. The position of the peak is at $f = f_0$. The half width of the peak (after it is de-skewed) is given as Δ (at relative height $1/e$), and the factor γ measures how much the peak is skewed towards larger f values (respectively lesser f values, if $s = -1$), with a direct interpretation in terms of the horizontal shift of the sides of the peak.

Appendix D: Confidence regions from the distribution $\mu(f)$

Here we see how to construct confidence regions from the histogram obtained by our method. As explained in the main text, regions with high weight in state space may be promoted to confidence regions by the method of Christandl and Renner.

Consider the region with all states ρ which have at least a given value of the figure of merit:

$$R_f = \{ \rho : f(\rho) \geq f \}. \quad (\text{D1})$$

The direction of the inequality in (D1) depends on which figures of merit are considered desirable. The direction used here reflects the fidelity to a target state, in which case higher fidelities are desirable. If, e.g., a proper distance measure such as the trace distance is used, the opposite inequality is preferable.

It is straightforward to see that the weight of the region R_f in state space according to the measure $\mu_{B^n}(\rho) d\rho$ is directly given by the weight of the function $\mu(f)$ over the corresponding range of f values which are included in the region R_f . For example, if the figure of merit is the fidelity to a target state, the weight $\alpha(f)$ of the region R_f is given by

$$\alpha(f) = \int_{\rho \in R_f} d\rho \mu_{B^n}(\rho) = \int_f^1 df' \mu(f'). \quad (\text{D2})$$

The value of f required for a region R_f to encompass a particular weight $1 - \varepsilon/\text{poly}(n)$ is thus given by inverting (D2). This may either be done directly from the numerical histogram points, or from a fit model. This gives us a region with high weight with respect to $\mu_{B^n}(\rho)$.

The method of Christandl and Renner may now be used to upgrade these regions to confidence regions. Choose a confidence level $1 - \varepsilon$, and calculate the corresponding $\text{poly}(n)$ and δ as given in ref. [28]. Recall that a region with weight $1 - \varepsilon/\text{poly}(n)$, once enlarged by δ in purified distance, is a confidence region with confidence $1 - \varepsilon$.

In general, the δ -enlargement can be translated into a cost in the corresponding bounding figure of merit f . We'll derive here this cost for our particular cases of interest of the fidelity to a pure reference state, the expectation value of an observable and the trace distance to any reference state. Consider first the case where the figure of merit corresponds to the trace distance to a reference state ρ_{Ref} , $f(\rho) = D(\rho, \rho_{\text{Ref}}) = \frac{1}{2} \|\rho - \rho_{\text{Ref}}\|_1$. Note the reverse inequality is used in (D1). Then, consider the region $R_{f+\delta}$. Now, we'll see that $R_{f+\delta}$ contains the set R_f enlarged by δ in purified distance. Indeed, if $\rho \in R_f$, and σ is such that $P(\rho, \sigma) = \sqrt{1 - F^2(\rho, \sigma)} \leq \delta$, then we may use the triangle inequality, along with the fact that $D(\rho, \sigma) \leq P(\rho, \sigma)$ [91], to see that $D(\sigma, \rho_{\text{Ref}}) \leq f + \delta$, and deduce that $\sigma \in R_{f+\delta}$. Thus, if R_f is a region with weight $1 - \varepsilon/\text{poly}(n)$, then $R_{f+\delta}$ is a confidence region of confidence level at least $1 - \varepsilon$. This construction is depicted graphically in Fig. 6. Of course, the same reasoning applies to the case where $f(\rho) = P(\rho, \rho_{\text{Ref}})$ is the purified distance to a reference state.

Consider also the case where $f(\rho) = \text{tr}(\rho W)$ is the expectation of an observable W . First, assume that the reverse inequality direction is used in (D1). Then the δ -enlargement of R_f is included in the region $R_{f+w\delta}$, where we've assumed that the eigenvalues z_j of W lie within an interval of size w , i.e. $w_- \leq z_j \leq w_+$ and $w = w_+ - w_-$, or equivalently, $w_- \mathbb{1} \leq W \leq w_+ \mathbb{1}$ and $w = w_+ - w_-$. Indeed, assume $f(\rho) \leq f$ and $P(\rho, \sigma) \leq \delta$. Then $D(\rho, \sigma) \leq P(\rho, \sigma)$ and by properties of the trace distance there exists $\Delta_{\pm} \geq 0$ such that $\sigma - \rho = \Delta_+ - \Delta_-$ and $\frac{1}{2} \text{tr}(\Delta_+ + \Delta_-) = \text{tr} \Delta_+ = \text{tr} \Delta_- = D(\rho, \sigma) \leq \delta$ [92]. Now, $f(\sigma) = \text{tr}(\sigma W) = f(\rho) + \text{tr}(\Delta_+ W) - \text{tr}(\Delta_- W) \leq f + w_+ \text{tr} \Delta_+ - w_- \text{tr} \Delta_- \leq f + w\delta$, and $\sigma \in R_{f+w\delta}$. If the forward direction inequality is used in (D1) instead of the reverse, then the same argument above is easily adapted to show that the δ -enlargement of R_f is included in the region $R_{f-w\delta}$, where w is defined in the same way.

Note also that the case of the squared fidelity to a pure reference state $|\psi_{\text{Ref}}\rangle$ is given by $f(\rho) = F^2(\rho, |\psi_{\text{Ref}}\rangle\langle\psi_{\text{Ref}}|) = \langle\psi_{\text{Ref}}|\rho|\psi_{\text{Ref}}\rangle$, and is thus the expectation value of the observable $|\psi_{\text{Ref}}\rangle\langle\psi_{\text{Ref}}|$. More precisely, we have $w_+ = 1$, $w_- = 0$ and $w = 1$, and the inequality direction used in (D1) encompasses larger values for the fidelity in the region; the enlarged set to consider is then simply $R_{f-\delta}$.

Remark that the error bars on the numerical estimate of $\mu(f)$, or on the relevant fit parameters, should *a priori* be propagated to the obtained confidence regions. However since $\mu(f)$ decays exponentially, small errors on the fit parameters will only have a negligible effect on the f required to contain a given weight $1 - \varepsilon/\text{poly}(n)$ as given by (D2). This is just like classical error bars—error bars hardly need their own error bars.

The final confidence regions obtained are still generally unmeaningfully large. For example, if we try to construct confidence regions for the two superconducting qubits and choose, say, $\varepsilon = 5\%$, then we see that $\varepsilon/\text{poly}(n) \sim 10^{-37}$. Yes, that's small.[93] The corresponding f required (see construction in Fig. 6) is $f \approx 0.85$, and we can calculate $\delta \sim 0.1$. The final confidence region comprises then all states with a fidelity to the target state in the range $[0.75, 1]$. This analysis is in itself

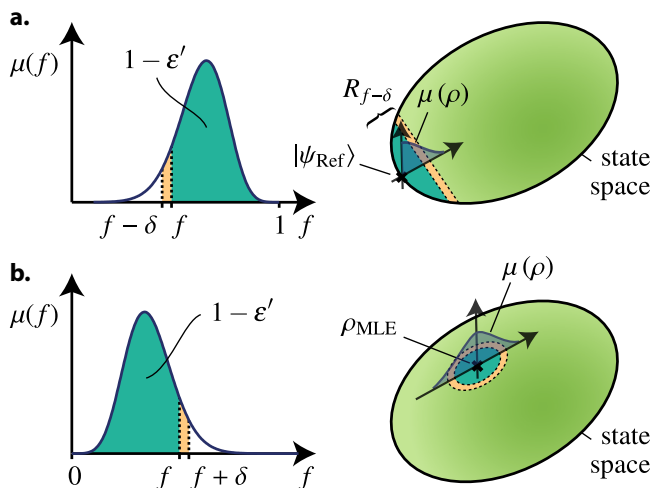


FIG. 6. Construction of confidence regions from the histogram of the figure of merit. High weight intervals with respect to $\mu(f)$ in the histogram plots (left plots) correspond to high weight regions in state space with respect to $\mu_{B^n}(\rho)$ (right diagrams). An appropriate enlargement by a parameter δ yields confidence regions. **a.** The case of the squared fidelity to a pure target state $|\psi_{\text{Ref}}\rangle$ as figure of merit, i.e. $f(\rho) = F^2(\rho, |\psi_{\text{Ref}}\rangle\langle\psi_{\text{Ref}}|) = \langle\psi_{\text{Ref}}|\rho|\psi_{\text{Ref}}\rangle$. An interval $[f, 1]$ in the histogram plot (turquoise region, left) corresponds to a region R_f in state space consisting of all states with squared fidelity to $|\psi_{\text{Ref}}\rangle$ higher than f (turquoise region, right). To construct a confidence region with a given confidence level $1 - \varepsilon$, first calculate $\varepsilon/\text{poly}(n)$ and δ as given in [28] and choose f such that the turquoise shaded area in the histogram plot is $1 - \varepsilon/\text{poly}(n)$. This means that the corresponding region R_f has weight at least $1 - \varepsilon/\text{poly}(n)$ under $\mu(\rho)$. Then, the region $R_{f-\delta}$ consisting of all states with squared fidelity at least $f - \delta$ to $|\psi_{\text{Ref}}\rangle$ form a confidence region of confidence level $1 - \varepsilon$ (turquoise and orange regions combined) [28]. The true state is almost surely in the region $R_{f-\delta}$; equivalently, the true fidelity to $|\psi_{\text{Ref}}\rangle$ is almost surely better than $f - \delta$. Observe that the regions constructed this way are linear slices of the quantum state space. This is because the squared fidelity to a pure state is linear. Also, the function $\mu(\rho)$ behaves approximately like a Gaussian around the maximum likelihood estimate ρ_{MLE} ; the illustration of $\mu(\rho)$ here corresponds to the case where ρ_{MLE} coincides with $|\psi_{\text{Ref}}\rangle\langle\psi_{\text{Ref}}|$. **b.** The analogous construction applied to the case where the figure of merit is the trace distance to the maximum likelihood estimate ρ_{MLE} . Here the regions R_f and $R_{f+\delta}$ are trace distance balls around ρ_{MLE} . If R_f has weight at least $1 - \varepsilon/\text{poly}(n)$, then $R_{f+\delta}$ is a confidence region of confidence level $1 - \varepsilon$.

not very useful, as it is fair to claim the experiment achieves considerably better precision than that (compare with Fig. 3 of the main text). The solution we propose is to provide a characterization of the full function $\mu(f)$ in terms of few parameters, from which we know that one can *in principle* construct confidence regions for any desired confidence level. This is very much akin to the error bars reported for a usual classical physical quantity: these may typically represent one standard deviation of a value which is assumed to be Gaussian distributed. A confidence region of high confidence level could then be much larger than the reported error bar. For example, a confidence level of one part in a million requires a region size of 5

standard deviations (or “5 sigma”).

Appendix E: Application of the method to simulated measurements

We have simulated measurements of individual Pauli operators on two qubits in the noisy entangled state

$$\rho = 0.95 |\Psi\rangle\langle\Psi| + 0.05 \frac{\mathbb{1}}{4}, \quad (\text{E1})$$

with the pure entangled state $|\Psi\rangle = (|01\rangle + i|10\rangle)/\sqrt{2}$. Each measurement setting consists of a pair of Pauli operators and has four outcomes, with a total of 9 measurement settings. Each setting was repeated 500 times, resulting in 4500 total measurement outcomes. Our procedure yields histograms corresponding to three different figures of merit (Fig. 7): (a) the fidelity to the state $|\Psi\rangle$, (b) the expectation value of an entanglement witness, and (c) the trace distance to the maximum likelihood estimate. The histograms were each generated with one random walk instance for each of the 12 CPU cores available. Each random walk produced 32768 samples, yielding a total of $12 \times 32768 = 393216$ recorded samples. Error bars were obtained by binning analysis for each run and combined with standard propagation of error bars. This analysis runs fast for two qubits and can usually be obtained within minutes on usual hardware.

For the figure of merit (a), we have $f(\rho) = F^2(\rho, |\Psi\rangle\langle\Psi|) = \langle\Psi|\rho|\Psi\rangle$. This figure of merit is often used to report the accuracy of experimental preparations of quantum states. Here the true value of this figure of merit is $F^2(\rho, |\Psi\rangle\langle\Psi|) = 0.9625$, given by the “true state” (E1) we used to simulate measurement outcomes. In (b), the figure of merit is $f(\rho) = \text{tr}(\rho W)$, with the entanglement witness $W = -\mathbb{1} - \sigma_X \otimes \sigma_Y + \sigma_Y \otimes \sigma_X - \sigma_Z \otimes \sigma_Z$. The operator W is chosen such that $\text{tr}(\rho W) \leq 0$ for all states ρ which are not entangled, but also such that $\text{tr}[|\Psi\rangle\langle\Psi|W] = 2$. For the last case considered, (c), we first calculate the maximum likelihood estimate ρ_{MLE} , and then define our figure of merit as $f(\rho) = D(\rho, \rho_{\text{MLE}})$, where $D(\rho, \sigma) := \frac{1}{2}\|\rho - \sigma\|_1$ is the trace distance. The eigenvalues of the density matrix ρ_{MLE} are $(0.000, 0.0105, 0.0240, 0.9655)$, meaning that the state lies on the border of state space.

Observe that the peak maxima in Fig. 7 do not correspond to the values of the maximum likelihood estimate ρ_{MLE} , even though the latter is precisely the point where $\mu_{B^n}(\rho)$ is maximal by definition. This is because of this increasing volume factor which shifts the peak. Indeed, at ρ_{MLE} we can evaluate $F^2(\rho_{\text{MLE}}, |\Psi\rangle\langle\Psi|) \approx 0.965$; the peak maximum in Figure 7a is clearly shifted.

Let us now apply the fit models to our numerical estimates. First, consider the trace distance as figure of merit. The corresponding theoretical model is (B8a) with $h = 0$, as given in Table I of the main text: $\ln \mu(f) \approx -a_2 f^2 - a_1 f + m \ln f + c$. The model fits well to the numerical estimate in Figure 7c (red curve). The fit was performed on the logarithm of the histogram. We used weights for each point obtained by propagating the error bars as $\Delta[\ln \mu] = |\partial(\ln \mu)/\partial \mu| \Delta \mu = \Delta \mu / \mu$.

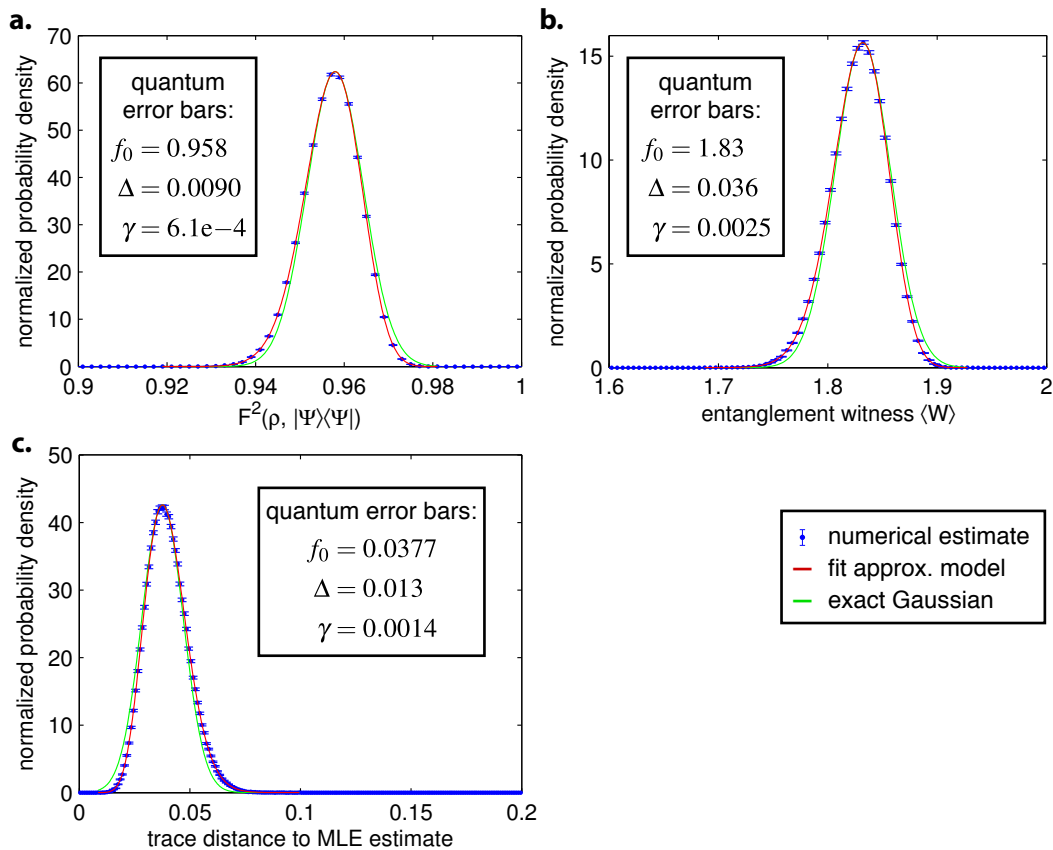


FIG. 7. Simulated example data analyzed using our procedure, along with the quantum error bars. Two qubits in a noisy entangled state were measured with individual Pauli operators. **a.** Histogram of the squared fidelity to the target state $|\Psi\rangle$ under the distribution which is relevant for the construction of confidence regions using the method of Christandl and Renner [28]. The numerical estimate (blue points) were obtained using our procedure based on a Metropolis-Hastings random walk. The theoretical model fits the numerics well (red curve). The quantum error bars characterize the distinctive features of the curve, which is interpreted as applying a “skewing” operation on an exact Gaussian (green curve). Confidence regions may be constructed from this histogram by choosing regions with states that have a certain minimum fidelity to the target state, chosen such that the set has high weight with respect to this distribution. The true value of the squared fidelity of the state from which we have simulated measurements is in fact 0.963; the shift is due to the increasing volume factor towards lower fidelity values. **b.** The same analysis is applied to the case of the expectation value of an entanglement witness. The witness is chosen to have positive expectation value only for entangled states, with a maximum at the maximally entangled state $|\Psi\rangle$ where $\langle\Psi|W|\Psi\rangle = 2$. **c.** The same analysis is again repeated for the case where the figure of merit is the trace distance to the maximum likelihood estimate.

Points with obviously huge error bars were excluded from the fit. The raw fit for $\ln\mu(f)$ is presented in Fig. 8, along with a plot of the residuals. The corresponding fit parameters are (with 95% confidence bounds):

$$\begin{aligned} a_2 &= 722.8 \quad (635.5, 810.1) \\ a_1 &= 319.6 \quad (305.6, 333.6) \\ m &= 14.09 \quad (13.82, 14.36) \\ c &= 63.00 \quad (61.71, 64.3). \end{aligned} \quad (\text{E2})$$

The value m is close to $M - 1 = 14$, which is the value we would predict from (B6) without the $w[f, \Omega_0]$ term. This indicates that this latter volume factor is approximately constant in

this case. The quantum error bars can be obtained with (C13),

$$\begin{aligned} f_0 &= 0.0377 ; \\ \Delta &= 0.013 ; \\ \gamma &= 0.0014 . \end{aligned} \quad (\text{E3})$$

Our model also fits the numerically obtained histogram in Figures 7a and 7b well. For Figure 7a, the appropriate fit model is $\ln\mu(f) \approx -a_2(1-f)^2 - a_1(1-f) + m\ln(1-f) + c$, and for Figure 7b we have used the model $\ln\mu(f) \approx -a_2(2-f)^2 - a_1(2-f) + m\ln(2-f) + c$, as specified by Table I of the main text. The respective quantum error bars are indicated on the corresponding plots in Fig. 7.

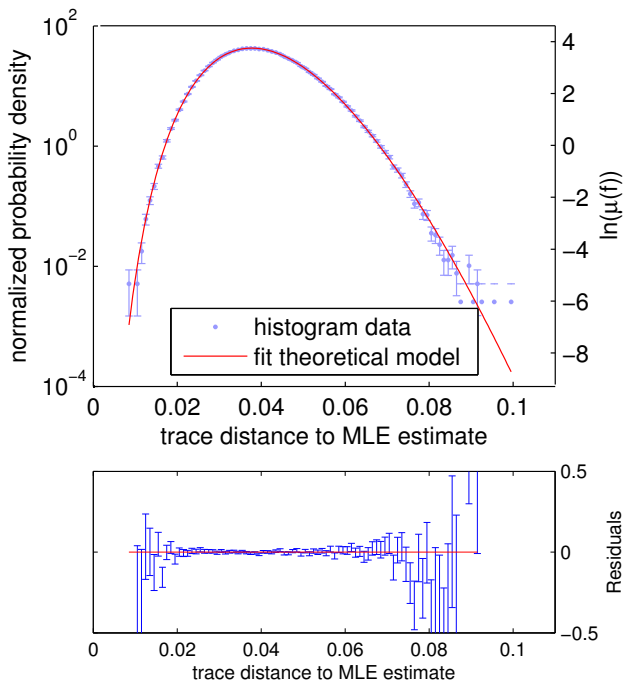


FIG. 8. Fit of the logarithm of the numerically obtained histogram. The log scale allows to better appreciate the quality of the fit. The bottom plot shows the residuals of the fit for $\ln \mu(f)$, that is, the difference between the logarithm of the numerical histogram points and the fitted model for the function $\ln \mu(f)$. The low deviation from zero for the central points underscores the quality of our model (and that the error bars may be overestimated). The points at the sides correspond to regions with very low probability and where the numerical estimate is anyway expected to be unreliable.

Appendix F: Application to experimental data and modeling noisy measurements

As an illustration, we apply our method to analyze measurement data obtained for two superconducting qubits in a Bell state prepared using the setup reported in [10]. The data were kindly provided by the authors of Ref. [10]. The measurement on an individual qubit is carried out by a transmission measurement on a resonator coupled to that qubit [78]. This measurement yields a random real value I which is distributed differently whether the qubit is in the $|0\rangle$ state or in the $|1\rangle$ state. Single-shot readouts are possible to reasonable accuracy using a simple threshold, because the two distributions of I corresponding to $|0\rangle$ and $|1\rangle$ have almost non-overlapping support [10]. However, we choose to model the measurement process more precisely, as our method assumes the POVM effects correctly incorporate any noise introduced by the measurement device itself. Here, we model the measurement process as a real-valued POVM. A calibration measurement yields the distributions $q_0(I)$ and $q_1(I)$ for trusted preparations of the $|0\rangle$ and $|1\rangle$ states respectively. The measurement of the Pauli operator σ_i is performed by applying the appropriate unitary gate U_i with high fidelity to bring the measurement basis onto the computational basis. The effects

corresponding to the real-valued POVM including the rotation with U_i are then

$$Q_i(I) = U_i^\dagger \begin{pmatrix} q_0(I) & 0 \\ 0 & q_1(I) \end{pmatrix} U_i. \quad (\text{F1})$$

(We have ignored here errors in implementing the gate U_i .) We could have used these POVM effects directly for each measured value for each qubit in the expression for the log-likelihood given by Eq. (2) of the main text, however for practical purposes (to reduce the number of different POVM effects), we have coarse-grained the values I into 20 different bins, yielding the discrete distributions $q'_0(k)$ and $q'_1(k)$ for bin number k . In other words, if the measured value I is in bin number k , then the corresponding POVM effect is

$$Q'_i(k) = U_i^\dagger \begin{pmatrix} q'_0(k) & 0 \\ 0 & q'_1(k) \end{pmatrix} U_i. \quad (\text{F2})$$

The joint POVM effect corresponding to combining individual measurements on the two qubits is simply given by tensoring the two POVM effects. For example, if the value I_A is measured on qubit A (falling in bin k_A) and the value I_B is measured on qubit B (which falls in the bin k_B), then the joint POVM effect is simply

$$Q'_{ij}(k_A, k_B) = Q'_i(k_A) \otimes Q'_j(k_B), \quad (\text{F3})$$

where U_i (resp. U_j) is the rotation applied to qubit A (resp. qubit B) before measuring the qubit in the computational basis.

We have analyzed the measurement data using the procedure described above. There were in total $n = 55677$ measurements. The histogram corresponding to the squared fidelity to the target Bell state is depicted in Fig. 3 of the main text. Our theoretical model (B8b) (with $h = 1$) fits the numerical estimate well. The fit parameters are (with 95% confidence bounds),

$$\begin{aligned} a_2 &= 8511 & (7909, 9112) \\ a_1 &= -476.8 & (-634.8, -318.7) \\ m &= 42.53 & (37.36, 47.69) \\ c &= 125.4 & (103.5, 147.2). \end{aligned} \quad (\text{F4})$$

From these fit parameters, we finally derive the quantum error bars

$$\begin{aligned} f_0 &= 0.934; \\ \Delta &= 0.0086; \\ \gamma &= 1.4 \times 10^{-4}. \end{aligned} \quad (\text{F5})$$

Appendix G: Comparison with error bars from other methods

A currently used *ad hoc* technique for obtaining error bars is bootstrapping [22, 24, 27, 41, 79]. In our simulated experiment above, we have performed a simple parametric bootstrapping analysis for comparison. We have simulated new measurement outcomes from ρ_{MLE} , using the same amount of

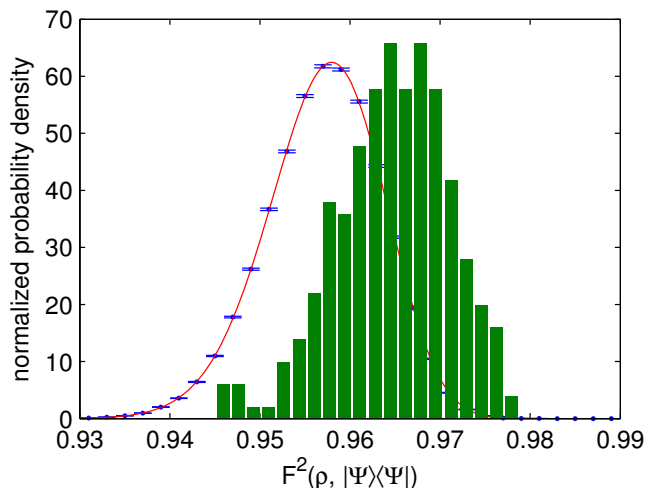


FIG. 9. Comparison with error bars from existing bootstrapping methods. The blue points and red curve reproduce the numerical estimate and fit in Figure 7a. We have resampled random measurement outcomes from the maximum likelihood estimate and plotted the resulting reconstructed squared fidelities to the target state $|\Psi\rangle$ (green histogram bars). The bias of the curve from our method is due to the increasing volume factor in the direction of lower fidelity values. We see here that our method yields error bars of the same order of magnitude as bootstrapping. However our error bars are well-justified, because they can serve to construct confidence regions for any confidence level.

measurements and the same settings as for the original simulated experiment. We repeated the procedure many times to obtain in total 300 new datasets. For each dataset, we have reconstructed the corresponding maximum likelihood estimate, and determined its squared fidelity to the target state $|\Psi\rangle$. The histogram of these values is presented in Fig. 9, compared with the result of our method in Figure 7a. We see that the width of the distribution is approximately the same. The bias of $\sim 1\%$ squared fidelity between the two methods is due to the increasing volume factor picked up by our method in the direction of decreasing fidelities. Our error bars, however, have the robust operational meaning as a means to construct confidence regions.

Appendix H: Discussion of the reliability of the method

In our work, we provide several levels of reliability statements. First, obviously if $\mu(f)$ can be exactly determined, then our error analysis is perfectly reliable, assuming the given measurement operators are accurate. In practice though, it is only possible to approximate $\mu(f)$ with numerical techniques. However these methods are standard and well-tested, and come with reliable error estimates [75]. Thus with minimal reasonable assumptions an error analysis based on this approximation of $\mu(f)$ is also reliable.

Furthermore, we provide an approximate theoretical model with only three fit parameters and which explains well the numerical estimate obtained. The quality of the fit over many

examples studied by the authors not only presents additional strong indication that the numerical estimate is faithful, but also shows that the result admits a simple representation with few parameters. Recall that the numerical method does not rely on the assumptions and approximations used to derive the theoretical fit model. Also, because of its form the fit model is relatively robust to small uncertainties in the fit parameters.

Our approximate fit model might fail though to describe the distribution accurately in some extreme cases, for example if too few measurements are taken (however examples with $n \sim 100$ total measurements were well fit). The model is also known not to apply to figures of merit such as the fidelity to a non-pure state, or more generally, figures of merit which do not satisfy (B5). However, the fit in these cases is usually of bad quality, especially in the region of the peak. In practice, it is sufficient to rely on goodness-of-fit measures or visual inspection of the quality of the fit to assert its validity.

Appendix I: Overview of our software

We are releasing a software suite which accomplishes our procedure in a wide range of settings [83]. The project is composed of a program ready for use, which is built upon a modular, generic C++ framework designed for flexibility and speed.

We expect our program to be directly usable in most experimental applications. Our program takes as input a list of POVM effects E_k , which are assumed to be independent, and a list of frequencies n_k which indicate how many times each corresponding POVM effect was observed. Further inputs include settings for the histogram range and number of bins, which figure of merit to use, parameters of the Metropolis-Hastings random walk, the number of times to repeat the random walk, the error analysis method, etc. The output of the program is the histogram as displayed for example in Fig. 7, as well as Fig. 3 of the main text, with corresponding error bars. We refer to the project's hosted location [83] for further documentation and detailed information about its usage. The histograms presented in this work were all obtained using our software.

This program is itself built upon a generic C++ framework with a collection of tools which may be used to specialize our method to more complex setups. We provide for example tools to specify the data for a quantum tomography problem, an implementation of an abstract Metropolis-Hastings random walk, an interface to collect statistics during this random walk, as well as tools for parallel processing several random walk instances. The code is written using a technique called C++ template metaprogramming [94], which allows to write generic code which is flexible and reusable, but which at compile-time is translated into highly optimized low-level machine instructions. Our project relies on the Eigen and Boost libraries [95, 96], in particular for linear algebra calculations. These libraries also make extensive use of this technique.

Some tasks are not covered by our program. If required by the figure of merit, finding the maximum likelihood estimate ρ_{MLE} can be accomplished by minimizing the loglikelihood $\lambda(\rho)$. Since this function is convex, the solution can

be found efficiently. In most of our examples, we used CVX, a MATLAB package for specifying and solving convex problems [97, 98]. Also, in order to determine the fit parameters corresponding to the histogram, we resorted to MATLAB's curve fitting toolbox. A MATLAB script is provided along with the software to ease this task, and to calculate the quantum error bars.

Our program is currently limited to POVM effects with a product structure. However, this is generically the case, even e.g. for adaptive tomography [99–101]. We have successfully used our code to analyze simulated measurements of Pauli operators of up to at least 5 qubits on our hardware, and we expect further improvements will increase this limit.

* pfaist@phys.ethz.ch

- [1] C. H. Bennett and D. P. DiVincenzo, *Nature* **404**, 247 (2000).
- [2] J. P. Home, in *Advances In Atomic, Molecular, and Optical Physics*, Vol. 62 (Elsevier, 2013) pp. 231–277, arXiv:1306.5950 [quant-ph].
- [3] M. H. Devoret and R. J. Schoelkopf, *Science* **339**, 1169 (2013).
- [4] T. E. Northup and R. Blatt, *Nature Photonics* **8**, 356 (2014).
- [5] M. F. Riedel, P. Böhi, Y. Li, T. W. Hänsch, A. Sinatra, and P. Treutlein, *Nature* **464**, 1170 (2010), arXiv:1003.1651 [quant-ph].
- [6] T. Monz, P. Schindler, J. T. Barreiro, M. Chwalla, D. Nigg, W. A. Coish, M. Harlander, W. Hänsel, M. Hennrich, and R. Blatt, *Physical Review Letters* **106**, 130506 (2011), arXiv:1009.6126 [quant-ph].
- [7] P. C. Maurer, G. Kucsko, C. Latta, L. Jiang, N. Y. Yao, S. D. Bennett, F. Pastawski, D. Hunger, N. Chisholm, M. Markham, D. J. Twitchen, J. I. Cirac, and M. D. Lukin, *Science* **336**, 1283 (2012).
- [8] I. Usmani, C. Clausen, F. Bussi eres, N. Sangouard, M. Afzelius, and N. Gisin, *Nature Photonics* **6**, 234 (2012), arXiv:1109.0440 [quant-ph].
- [9] A. Fedorov, L. Steffen, M. Baur, M. P. da Silva, and A. Wallraff, *Nature* **481**, 170 (2012), arXiv:1108.3966 [quant-ph].
- [10] L. Steffen, Y. Salathe, M. Oppliger, P. Kurpiers, M. Baur, C. Lang, C. Eichler, G. Puebla-Hellmann, A. Fedorov, and A. Wallraff, *Nature* **500**, 319 (2013), arXiv:1302.5621 [quant-ph].
- [11] F. Bussi eres, C. Clausen, A. Tiranov, B. Korzh, V. B. Verma, S. W. Nam, F. Marsili, A. Ferrier, P. Goldner, H. Herrmann, C. Silberhorn, W. Sohler, M. Afzelius, and N. Gisin, *Nature Photonics* **8**, 775 (2014), arXiv:1401.6958 [quant-ph].
- [12] T. P. Harty, D. T. C. Allcock, C. J. Ballance, L. Guidoni, H. A. Janacek, N. M. Linke, D. N. Stacey, and D. M. Lucas, *Physical Review Letters* **113**, 220501 (2014), arXiv:1403.1524 [quant-ph].
- [13] C. W. Helstrom, *Journal of Statistical Physics* **1**, 231 (1969).
- [14] K. Vogel and H. Risken, *Physical Review A* **40**, 2847 (1989).
- [15] G. M. D'Ariano, *Physics Letters A* **268**, 151 (2000).
- [16] G. Cassinelli, G. M. D'Ariano, E. De Vito, and A. Leverero, *Journal of Mathematical Physics* **41**, 7940 (2000), arXiv:quant-ph/0004026 [quant-ph].
- [17] R. T. Thew, A. G. White, and W. J. Munro, *Physical Review A* **66**, 12303 (2002), arXiv:quant-ph/0201052 [quant-ph].
- [18] G. M. D'Ariano, M. G. A. Paris, and M. F. Sacchi, *Advances in Imaging and Electron Physics* **128**, 205 (2003), arXiv:quant-ph/0302028 [quant-ph].
- [19] M. Paris and J. Řeháček, eds., *Quantum State Estimation*, Lecture Notes in Physics, Vol. 649 (Springer, Berlin, Heidelberg, 2004).
- [20] Z. Hradil, *Physical Review A* **55**, R1561 (1997).
- [21] J. Řeháček, Z. Hradil, and M. Je ek, *Physical Review A* **63**, 40303 (2001), arXiv:quant-ph/0009093 [quant-ph].
- [22] B. Efron and R. J. Tibshirani, *An Introduction to the Bootstrap* (CRC Press, 1994) p. 456.
- [23] D. F. V. James, P. G. Kwiat, W. J. Munro, and A. G. White, *Physical Review A* **64**, 52312 (2001).
- [24] J. P. Home, D. Hanneke, J. D. Jost, J. M. Amini, D. Leibfried, and D. J. Wineland, *Science* **325**, 1227 (2009), arXiv:0907.1865 [quant-ph].
- [25] R. Blume-Kohout, *New Journal of Physics* **12**, 043034 (2010), arXiv:quant-ph/0611080 [quant-ph].
- [26] B. Jungnitsch, S. Niekamp, M. Kleinmann, O. G uhne, H. Lu, W.-B. Gao, Y.-A. Chen, Z.-B. Chen, and J.-W. Pan, *Physical Review Letters* **104**, 210401 (2010), arXiv:0912.0645 [quant-ph].
- [27] R. Blume-Kohout, ArXiv e-prints (2012), arXiv:1202.5270 [quant-ph].
- [28] M. Christandl and R. Renner, *Physical Review Letters* **109**, 120403 (2012), arXiv:1108.5329 [quant-ph].
- [29] J. M. Arrazola, O. Gittsovich, J. M. Donohue, J. Lavoie, K. J. Resch, and N. L utkenhaus, *Physical Review A* **87**, 062331 (2013), arXiv:1302.1182 [quant-ph].
- [30] T. Kiesel, W. Vogel, V. Parigi, A. Zavatta, and M. Bellini, *Physical Review A* **78**, 021804 (2008), arXiv:0804.1016 [quant-ph].
- [31] J. Řeháček, D. Mogilevtsev, and Z. Hradil, *New Journal of Physics* **10**, 43022 (2008).
- [32] T. Kiesel and W. Vogel, *Physical Review A* **82**, 032107 (2010), arXiv:1004.0788 [quant-ph].
- [33] R. Blume-Kohout, J. O. S. Yin, and S. J. van Enk, *Physical Review Letters* **105**, 170501 (2010), arXiv:1005.0003 [quant-ph].
- [34] R. Blume-Kohout, *Physical Review Letters* **105**, 200504 (2010).
- [35] T. Sugiyama, P. Turner, and M. Mura, *Physical Review A* **83**, 12105 (2011), arXiv:1009.2164 [quant-ph].
- [36] C. Ferrie and R. Blume-Kohout, *AIP Conference Proceedings* **1443**, 10 (2012), arXiv:1201.1493 [math.ST].
- [37] D. Rosset, R. Ferretti-Sch obitz, J.-D. Bancal, N. Gisin, and Y.-C. Liang, *Physical Review A* **86**, 062325 (2012), arXiv:1203.0911 [quant-ph].
- [38] J. Shang, H. K. Ng, A. Schrawat, X. Li, and B.-G. Englert, *New Journal of Physics* **15**, 123026 (2013), arXiv:1302.4081 [quant-ph].
- [39] M. Walter and J. M. Renes, *IEEE Transactions on Information Theory* **60**, 8007 (2014), arXiv:1310.2155 [quant-ph].
- [40] T. Sugiyama, *Physical Review A* **91**, 042126 (2015), arXiv:1407.8065 [quant-ph].
- [41] C. Schwemmer, L. Knips, D. Richart, H. Weinfurter, T. Moroder, M. Kleinmann, and O. G uhne, *Physical Review Letters* **114**, 080403 (2015), arXiv:1310.8465 [quant-ph].
- [42] H. Ball, T. M. Stace, S. T. Flammia, and M. J. Biercuk, *Physical Review A* **93**, 022303 (2016), arXiv:1504.05307 [quant-ph].

- ph].
- [43] A. I. Lvovsky, *Journal of Optics B: Quantum and Semiclassical Optics* **6**, S556 (2004), arXiv:quant-ph/0311097 [quant-ph].
- [44] R. Blume-Kohout and P. Hayden, ArXiv e-prints (2006), arXiv:quant-ph/0603116 [quant-ph].
- [45] R. Schmied and P. Treutlein, *New Journal of Physics* **13**, 065019 (2011), arXiv:1101.4131 [quant-ph].
- [46] K. Dobek, M. Karpiński, R. Demkowicz-Dobrzański, K. Banaszek, and P. Horodecki, *Physical Review Letters* **106**, 030501 (2011), arXiv:1010.4575 [quant-ph].
- [47] J. Smolin, J. Gambetta, and G. Smith, *Physical Review Letters* **108**, 70502 (2012), arXiv:1106.5458 [quant-ph].
- [48] A. Anis and A. I. Lvovsky, *New Journal of Physics* **14**, 105021 (2012), arXiv:1204.5936 [quant-ph].
- [49] R. D. Gill and M. I. Gutf, in *From Probability to Statistics and Back: High-Dimensional Models and Processes – A Festschrift in Honor of Jon A. Wellner*, Collections, Vol. 9, edited by M. Banerjee, F. Bunea, J. Huang, V. Koltchinskii, and M. H. Maathuis (Institute of Mathematical Statistics, Beachwood, Ohio, USA, 2013) pp. 105–127, arXiv:1112.2078 [quant-ph].
- [50] M. Kech, P. Vrana, and M. M. Wolf, *Journal of Physics A: Mathematical and Theoretical* **48**, 265303 (2015), arXiv:1503.00506 [quant-ph].
- [51] G. Haack, A. Steffens, J. Eisert, and R. Hübener, ArXiv e-prints (2015), arXiv:1504.04194 [quant-ph].
- [52] A. Carpentier, J. Eisert, D. Gross, and R. Nickl, ArXiv e-prints (2015), arXiv:1504.03234 [math.ST].
- [53] J. Haah, A. W. Harrow, Z. Ji, X. Wu, and N. Yu, ArXiv e-prints (2015), arXiv:1508.01797 [quant-ph].
- [54] R. O’Donnell and J. Wright, ArXiv e-prints (2015), arXiv:1508.01907 [quant-ph].
- [55] J. Řeháček, Z. Hradil, E. Knill, and A. Lvovsky, *Physical Review A* **75**, 42108 (2007), arXiv:quant-ph/0611244 [quant-ph].
- [56] R. Kueng and C. Ferrie, *New Journal of Physics* **17**, 123013 (2015), arXiv:1503.00677 [quant-ph].
- [57] C. Granade, J. Combes, and D. G. Cory, *New Journal of Physics* **18**, 033024 (2016), arXiv:1509.03770 [quant-ph].
- [58] M. P. da Silva, O. Landon-Cardinal, and D. Poulin, *Physical Review Letters* **107**, 210404 (2011), arXiv:1104.3835 [quant-ph].
- [59] S. T. Flammia and Y.-K. Liu, *Physical Review Letters* **106**, 230501 (2011), arXiv:1104.4695 [quant-ph].
- [60] M. Cramer, M. B. Plenio, S. T. Flammia, R. Somma, D. Gross, S. D. Bartlett, O. Landon-Cardinal, D. Poulin, and Y.-K. Liu, *Nature communications* **1**, 149 (2010), arXiv:1101.4366 [quant-ph].
- [61] D. Gross, Y.-K. Liu, S. Flammia, S. Becker, and J. Eisert, *Physical Review Letters* **105**, 150401 (2010), arXiv:0909.3304 [quant-ph].
- [62] S. T. Flammia, D. Gross, Y.-K. Liu, and J. Eisert, *New Journal of Physics* **14**, 095022 (2012), arXiv:1205.2300 [quant-ph].
- [63] G. Tóth, W. Wieczorek, D. Gross, R. Krischek, C. Schwemmer, and H. Weinfurter, *Physical Review Letters* **105**, 250403 (2010), arXiv:1005.3313 [quant-ph].
- [64] T. Moroder, P. Hyllus, G. Tóth, C. Schwemmer, A. Niggelbaum, S. Gaile, O. Gühne, and H. Weinfurter, *New Journal of Physics* **14**, 105001 (2012), arXiv:1205.4941 [quant-ph].
- [65] C. Schwemmer, G. Tóth, A. Niggelbaum, T. Moroder, D. Gross, O. Gühne, and H. Weinfurter, *Physical Review Letters* **113**, 040503 (2014), arXiv:1401.7526 [quant-ph].
- [66] In the general case considered in Ref. [28], the measurements need not be independent, and the underlying quantum state of the n systems only needs to be permutation-invariant. We focus on the case of independent measurements for clarity of presentation and since this situation is the most widespread, although the results are expected to hold in the general case as well.
- [67] We use the notation of Ref. [28]; there, the general case of a joint measurement on the n systems is considered and the outcome POVM effect is denoted by B^n .
- [68] I. Bengtsson and K. Życzkowski, *Geometry of Quantum States: An Introduction to Quantum Entanglement* (Cambridge University Press, Cambridge, UK, 2006).
- [69] K. Życzkowski and H.-J. Sommers, *Journal of Physics A* **34**, 7111 (2001), arXiv:quant-ph/0012101 [quant-ph].
- [70] The output region should in fact be R^δ , obtained by enlarging the set R by some small δ in fidelity distance; explicit expressions for $\text{poly}(n)$ and δ are given in Ref. [28].
- [71] N. Metropolis, A. W. Rosenbluth, M. N. Rosenbluth, A. H. Teller, and E. Teller, *The Journal of Chemical Physics* **21**, 1087 (1953).
- [72] J. Shang, Y.-L. Seah, H. K. Ng, D. J. Nott, and B.-G. Englert, *New Journal of Physics* **17**, 043017 (2015), arXiv:1407.7805 [quant-ph].
- [73] Y.-L. Seah, J. Shang, H. K. Ng, D. J. Nott, and B.-G. Englert, *New Journal of Physics* **17**, 043018 (2015), arXiv:1407.7806 [quant-ph].
- [74] A. F. Albuquerque, F. Alet, P. Corboz, P. Dayal, A. Feiguin, S. Fuchs, L. Gamper, E. Gull, S. Gürtler, A. Honecker, R. Igarashi, M. Körner, A. Kozhevnikov, A. Läuchli, S. R. Manmana, M. Matsumoto, I. P. McCulloch, F. Michel, R. M. Noack, G. Pawłowski, L. Pollet, T. Pruschke, U. Schollwöck, S. Todo, S. Trebst, M. Troyer, P. Werner, and S. Wessel, *Journal of Magnetism and Magnetic Materials* **310**, 1187 (2007), arXiv:0801.1765 [cond-mat.str-el].
- [75] V. Ambegaokar and M. Troyer, *American Journal of Physics* **78**, 150 (2010), arXiv:0906.0943 [physics.comp-ph].
- [76] We assume that not too few measurements have been taken, and invoke some approximation methods such as Laplace’s method for integrating an exponential (see details in Appendix B).
- [77] M. Baur, A. Fedorov, L. Steffen, S. Philipp, M. P. Da Silva, and A. Wallraff, *Physical Review Letters* **108**, 1 (2012), arXiv:1107.4774 [quant-ph].
- [78] R. Bianchetti, S. Philipp, M. Baur, J. Fink, M. Göppl, P. Leek, L. Steffen, A. Blais, and A. Wallraff, *Physical Review A* **80**, 43840 (2009).
- [79] M. W. Mitchell, C. W. Ellenor, S. Schneider, and A. M. Steinberg, *Physical Review Letters* **91**, 120402 (2003).
- [80] C. Stark, *Physical Review A* **89**, 052109 (2014), arXiv:1209.5737 [quant-ph].
- [81] C. Stark, ArXiv e-prints (2012), arXiv:1209.6499 [quant-ph].
- [82] C. Stark, ArXiv e-prints (2012), arXiv:1210.1105 [quant-ph].
- [83] P. Faist, “The Tomographer project,” <https://github.com/Tomographer/tomographer/> (2015).
- [84] M. Tomamichel, C. C. W. Lim, N. Gisin, and R. Renner, *Nature communications* **3**, 634 (2012), arXiv:1103.4130 [quant-ph].
- [85] I. L. Chuang and M. A. Nielsen, *Journal of Modern Optics* **44**, 2455 (1997).
- [86] J. L. O’Brien, G. J. Pryde, A. Gilchrist, D. F. V. James, N. K. Langford, T. C. Ralph, and A. G. White, *Physical Review Letters* **93**, 080502 (2004), arXiv:quant-ph/0402166 [quant-ph].
- [87] R. A. Bertlmann and P. Kramer, *Journal of Physics A: Mathematical and Theoretical* **41**, 235303 (2008), arXiv:0806.1174

- [quant-ph].
- [88] E. Brüning, H. Mäkelä, A. Messina, and F. Petruccione, *Journal of Modern Optics* **59**, 1 (2012), arXiv:1103.4542 [quant-ph].
- [89] G. Kimura, *Physics Letters A* **314**, 339 (2003), arXiv:quant-ph/0301152 [quant-ph].
- [90] M. S. Byrd and N. Khaneja, *Physical Review A* **68**, 062322 (2003), arXiv:quant-ph/0302024 [quant-ph].
- [91] M. Tomamichel, R. Colbeck, and R. Renner, *IEEE Transactions on Information Theory* **56**, 4674 (2010), arXiv:0907.5238 [quant-ph].
- [92] M. M. Wilde, *Quantum Information Theory* (Cambridge University Press, 2013) p. 642, arXiv:1106.1445 [quant-ph].
- [93] This figure even uses an improved polynomial factor $\text{poly}(n) = 2n^{(d^2-1)/2}$ [102] over the original one in Ref. [28].
- [94] A. Alexandrescu, *Modern C++ Design: Generic Programming and Design Patterns Applied* (Addison-Wesley Professional, 2001) p. 323.
- [95] G. Guennebaud, B. Jacob, and Others, “Eigen v3,” (2010).
- [96] “Boost libraries,” (2015).
- [97] M. Grant and S. Boyd, in *Recent Advances in Learning and Control*, Lecture Notes in Control and Information Sciences, edited by V. Blondel, S. Boyd, and H. Kimura (Springer-Verlag Limited, 2008) pp. 95–110.
- [98] M. Grant and S. Boyd, “CVX: Matlab software for disciplined convex programming, version 2.1,” (2014).
- [99] Y. Teo, B.-G. Englert, J. Řeháček, and Z. Hradil, *Physical Review A* **84**, 62125 (2011), arXiv:1110.1202 [quant-ph].
- [100] T. Sugiyama, P. S. Turner, and M. Muraio, *Physical Review A* **85**, 52107 (2012), arXiv:1203.3391 [quant-ph].
- [101] D. H. Mahler, L. A. Rozema, A. Darabi, C. Ferrie, R. Blume-Kohout, and A. M. Steinberg, *Physical Review Letters* **111**, 183601 (2013), arXiv:1303.0436 [quant-ph].
- [102] M. Christandl, (2012), private Communication.